Soft Matter

PAPER

Cite this: *Soft Matter*, 2019, **15**, 937

Pressure responsive gating in nanochannels coated by semiflexible polymer brushes

K. Speyer [ab] and C. Pastorino [*ab]

We study by coarse-grained molecular-dynamics simulations the liquid flow in a slit channel with the inner walls coated by semiflexible polymer brushes. The distance between walls is close enough such that polymers grafted to opposing walls interact among each other and form bundles across the channel in poor solvent conditions. The solvent is simulated explicitly, including particles that fill the interior of the channel. The system is studied in equilibrium and under flow, by applying a constant body force on each particle of the system. A non-linear relation between external force and flow rate is observed, for a particular set of parameters. This non-linear response is linked to a morphological change of the polymer brushes. For large enough forces, the bundle structures formed across the channel break as the chains lean in the direction of the flow, and clear the middle of the channel. This morphological alteration of the polymer configurations translates in a sudden increase in the flow rate, acting as a pressure-responsive gate. The relation between flow and external force is investigated for various parameters, such as grafting density, quality of the solvent and polymer bending rigidity. We observe a non-monotonic dependence of the flow as a function of the polymer rigidity, and find an optimum value for the persistence length. We also find that the force threshold at which the morphological changes happen in the polymer brush, depends linearly on the grafting density. These findings can lead to new flow control techniques in micro and nano-fluidic devices.

Received 23rd November 2018,
Accepted 2nd January 2019

DOI: 10.1039/c8sm02388c

rsc.li/soft-matter-journal

I. Introduction

Controlling liquid flow in high confinement is crucial to develop new technological applications in the growing field of nano and microfluidics. A strategy that proved to be successful in this direction is coating the walls of nanochannels with "smart" materials. Polymer brushes have demonstrated to be a versatile substrate capable of high functionalization of surfaces for a variety of applications, like wetting, corrosion control and colloid stabilization.[1] The extensive use of polymer brushes is due to their flexibility to create stable thin films in which chemical composition, thickness and grafting density can be controlled and even addressed with nanoscale precision using well-established experimental methods.

Polymer brushes in nanopores provide a high selectivity tool for a variety of applications for flow control acting as valves. Tethering polymers to the interior walls of a nano-channel, allows to abruptly switch the flow rate by inducing morphological changes in the system *via* an external stimuli, such as pH, temperature or light conditions. These devices work very much like transistors do in electrical circuits, where the conductivity through the transistor is controlled by applying a voltage to one pair of its terminals. Fortin and Klok reported a hydraulic flow sensor prototype using glucose-responsive polymer brushes that swell upon binding with the target molecule.[2] Yameen *et al.* designed brush-coated conical nanopores to obtain a highly functional signal-responsive chemical nano-device.[3] In this case, the responsive brushes were constituted of zwitterionic monomers whose charge is regulated *via* changes of pH in the environmental conditions. Temperature activated nano-valves have also been investigated theoretically[4] and experimentally[5] observing a high sensitivity of the gate. These results lead to great advances towards the development of nano-medical devices, in which transport of an encapsulated drug across a polymer coated nanopore is regulated based on a change in a given physiologic parameter.[6–9]

Flow confined by polymer brushes is not only found in technological applications. The endothelial glycocalyx, present in blood vessels, is a perfect example of the importance of the brush-liquid interplay in nature. Furthermore, various groups have been investigating theoretically and experimentally these systems, to elucidate the influence of the "hairy" structures on the fluid inside microchannels.[10–14] Lanotte *et al.*[15] studied the flow behavior of red blood cells in glass microcapillaries, coated with a polymer brush, and found that the glycocalyx

[a] *Departamento de Física de la Materia Condensada, Centro Atómico Constituyentes, CNEA, Av. Gral. Paz 1499, 1650 Pcia. de Buenos Aires, Argentina. E-mail: pastor@cnea.gov.ar*
[b] *CONICET, Godoy Cruz 2290 (C1425FQB), Buenos Aires, Argentina*

is the main factor responsible of the higher flow resistance found *in vivo*.

A widely studied example of gating in nanochannels is the solvent-controlled nanopore, in which the gate can be opened or closed by a change in the quality of the solvent.[6,16–23] In these systems, the tethered polymers undergo a coil-to-globule transition as the external stimuli is applied, which obstructs or facilitates the passage of fluid across the channel. The switch between the open state and a closed-pore state is expressed in an abrupt decay of the flow rate. Several experimentally available parameters (grafting density, channel width, length of the polymers) can be explored to maximize the sensitivity of the system upon changes on the stimuli.

Adiga *et al.*[6,16–18] have been studying flow gating through polymer grafted nanopores for more than a decade, exploring different channel geometries and solvent conditions. In a cylindrical channel, they observed a linear increase in the permeability upon increasing the driving force in good solvent conditions, which provides a flow control mechanism. This enhancement in the flow is explained by a reduction in the polymer brush height due to the coil-to-globule transition, and a concomitant increase in the effective radius of the pore. In order for this transition to occur, the shear flow has to be stronger than the restoring entropic force of the fully flexible polymers. Huang *et al.* studied gating in a slit-like nanochannel coated with polymer brushes, as the solvent quality was varied, for various grafting densities and chain lengths.[19] Although they observed an increase in the permeability as the pressure drop increased in poor solvent, there was no decrease in the brush height.

Much attention has been given to nano-valves composed of fully flexible polymer brushes, but to the best of our knowledge, there is no comprehensive study of the influence of the chains' stiffness on the gating process. Previous studies show that, as the stiffness of the polymers increases, there is an associated change in the morphology of the brush, and the rheological properties are modified substantially.[24–26] Conformational changes in the polymer brush influence greatly the flow through nano-channels.[27,28] This suggests that the stiffness of the polymeric chains can have a considerable effect in the brush-solvent interplay in the gating process, which can lead to new and more efficient flow control mechanisms. In this work we study the open/close switching in a slit-like nano-channel coated with semiflexible polymers, as a function of the shear rate. The top- and bottom-grafted polymers meet in the middle of the channel, forming bundle structures which fill the interior of the pore together with the liquid. The affinity between brush and liquid is selected to reproduce a solvophobic system that favors the formation of these polymeric structures. This system is also known to produce liquid nanopatterning with brushes comprised of fully flexible chains.[29] When a small constant force is applied on the system particles, the bundles obstruct the flow, and the liquid velocity is low. Upon increasing the applied force, the bundle structures break and the brush height decreases, leaving the center of the channel available for the liquid, which leads to a sudden increase in the flow rate, as depicted in Fig. 1.

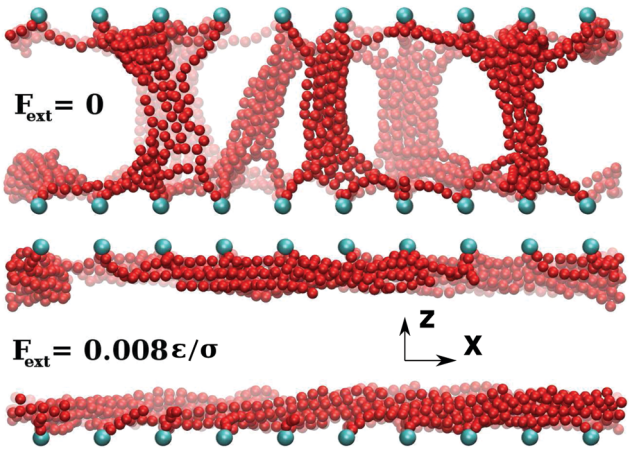

Fig. 1 Snapshots of the nano-channel coated with polymer brushes. Solvent particles that fill the channel are not shown for clarity. Up: The top- and bottom-grafted polymers form bundle structures that obstruct the flow inside the channel. Down: Upon imposing a sufficiently intense external force, the chains lean in the direction of the flow breaking the bundle structures and clearing the middle of the pore.

In the next Section II we go through the simulation technique and system details. The results are divided in three subsections. In sub-Section IIIA, we investigate the influence of the bending rigidity of the polymers on the gating process. In the sub-Section IIIB, we vary the number of tethered chains per surface area, to explore the effect of grafting density on the flow. In sub-Section IIIC, we change the liquid-polymer affinity to investigate the influence of the solvent quality in the nano-valve. Lastly, in Section IV, we give a brief summary of the results obtained in this work and our concluding remarks.

II. Simulation technique

Molecular dynamics simulations were carried out using the dissipative particle dynamics thermostat (DPD), to maintain a constant temperature. A coarse-grained model was chosen to speed up the simulations, while accounting for the important features in the system. In the DPD scheme, the forces over the i-th particle is calculated as:

$$\boldsymbol{F}_i = \sum_{j \neq i} \boldsymbol{F}_{ij}^{\mathrm{C}} + \boldsymbol{F}_{ij}^{\mathrm{D}} + \boldsymbol{F}_{ij}^{\mathrm{R}}, \tag{II.1}$$

where $\boldsymbol{F}_{ij}^{\mathrm{C}}$ is the conservative force that particle j exerts on particle i, which will be explained later. The other two terms, $\boldsymbol{F}_{ij}^{\mathrm{D}}$ and $\boldsymbol{F}_{ij}^{\mathrm{R}}$, are the dissipative and random forces respectively, which have the following expression:

$$\boldsymbol{F}_{ij}^{\mathrm{D}} = -\gamma \omega^{\mathrm{D}}(|\boldsymbol{r}_i - \boldsymbol{r}_j|)(\hat{\boldsymbol{r}}_{ij} \cdot \boldsymbol{v}_{ij})\hat{\boldsymbol{r}}_{ij} \tag{II.2}$$

$$\boldsymbol{F}_{ij}^{\mathrm{R}} = \zeta \omega^{\mathrm{R}}(|\boldsymbol{r}_i - \boldsymbol{r}_j|)\eta_{ij}\hat{\boldsymbol{r}}_{ij}, \tag{II.3}$$

where γ is the friction coefficient, ζ is the intensity of the thermal noise, $\boldsymbol{v}_{ij}$ is the velocity of particle i relative to particle j, $\hat{\boldsymbol{r}}_{ij}$ is the unit vector joining the positions of particles i and j, ω^{D} and ω^{R} are weight functions that depend on the distance

between the pair of particles, and η_{ij} is a random number generated for each occurrence, which fulfills:

$$\begin{cases} \langle \eta_{ij} \rangle = 0 \\ \left\langle \eta_{ij}(t)\eta_{kl}(t') \right\rangle = \left(\delta_{ik}\delta_{jl} + \delta_{il}\delta_{jk}\right)\delta_{tt'} \end{cases} \quad \text{(II.4)}$$

The functions ω^{D} and ω^{R} were chosen as usual:

$$\omega^{\mathrm{D}}(r) = \left[\omega^{\mathrm{R}}(r)\right]^2 = \begin{cases} \left(1 - r/r_{\mathrm{DPD}}\right)^2, & r \le r_{\mathrm{DPD}} \\ 0 & r > r_{\mathrm{DPD}} \end{cases}, \quad \text{(II.5)}$$

where r_{DPD} is the cutoff radius for the thermostat interactions. This choice, along with setting $\zeta^2 = 2\gamma k_{\mathrm{B}}T$, ensure that the fluctuation-dissipation relations are fulfilled.[30] The friction coefficient was set to $\gamma = 0.5$.

The model is comprised of three conservative force terms, in order to account for the polymer bending stiffness, the chain connectivity and excluded volume plus attractive interactions. The latter is modeled *via* a truncated and shifted Lennard-Jonnes potential:

$$U(r) = \begin{cases} U_{\mathrm{LJ}}(r) - U_{\mathrm{LJ}}(r_{\mathrm{C}}), & r \le r_{\mathrm{C}} \\ 0 & r > r_{\mathrm{C}} \end{cases} \quad \text{(II.6)}$$

where U_{LJ} is the Lennard-Jonnes potential given by:

$$U_{\mathrm{LJ}}(r) = 4\varepsilon_{\alpha\beta}\left[\left(\frac{\sigma}{r}\right)^{12} - \left(\frac{\sigma}{r}\right)^{6}\right] \quad \text{(II.7)}$$

The subindexes α, β stand for the different types of particles, which can be either solvent or monomer. Using distinct values of ε for monomer–monomer ($\varepsilon_{\mathrm{mm}}$), monomer–solvent ($\varepsilon_{\mathrm{ms}}$) and solvent–solvent ($\varepsilon_{\mathrm{ss}}$) allows to tune the affinity between liquid and polymers to explore different solvent qualities. These parameters were set to $\sigma = 1$ and $\varepsilon \equiv \varepsilon_{\mathrm{mm}} = \varepsilon_{\mathrm{ss}} = 1$, and are used as the distance and energy units respectively. All masses where set to $m = 1$ and the time units are defined in terms of these parameters as $\tau \equiv \sigma\sqrt{m/\varepsilon}$. The cut-off radius was set to twice the distance to the minimum, to include attractive interactions $r_{\mathrm{C}} = 2.24\sigma$, unless otherwise stated. For the thermostat interactions, the cut-off distance between particles was set to $r_{\mathrm{DPD}} = 2.24\sigma$ in every case. The temperature was fixed at $k_{\mathrm{B}}T = 0.8\varepsilon$, in order for the solvent to be in a liquid phase flowing through the channel.[31]

The connectivity of the polymeric chains is imposed *via* a finite extensible nonlinear elastic potential (FENE), given by:

$$U_{\mathrm{FENE}}(r) = \begin{cases} -\frac{1}{2}kr_0^2 \ln\left[1 - \left(\frac{r}{r_0}\right)^2\right], & r < r_0 \\ \infty & r \ge r_0 \end{cases} \quad \text{(II.8)}$$

where $k = 30\varepsilon/\sigma^2$, $r_0 = 1.5\sigma$. This model is the well studied Kremer–Grest model that correctly reproduces the dynamics of the polymer chains.[32,33]

A distinctive aspect of this work is the study of the influence of chains stiffness on the gating process. A quadratic bending potential was imposed between consecutive monomers, to account for this property of the polymers:

$$U_{\mathrm{bend}}(\theta) = \frac{1}{2}k_{\mathrm{b}}\theta^2, \quad \text{(II.9)}$$

where the bending constant k_{b} controls the rigidity of the polymer, and θ is the angle defined by:

$$\cos(\theta) = \frac{(\boldsymbol{r}_{i+1} - \boldsymbol{r}_i)(\boldsymbol{r}_i - \boldsymbol{r}_{i-1})}{|\boldsymbol{r}_{i+1} - \boldsymbol{r}_i||\boldsymbol{r}_i - \boldsymbol{r}_{i-1}|} \quad \text{(II.10)}$$

This potential was also used in order to orient the polymers in the direction perpendicular to the walls. An orientation force on the second bead is applied according to eqn (II.9), and the angle θ is calculated by setting $\boldsymbol{r}_{i-1} = \boldsymbol{r}_i - 1\sigma\hat{z}$ for the polymers grafted to the lower wall and $\boldsymbol{r}_{i-1} = \boldsymbol{r}_i + 1\sigma\hat{z}$ for the polymers grafted to the upper wall.

A convenient dimensionless magnitude to quantify the rigidity of a polymer is the ratio of its persistence length l_{p} over the contour length l_{c}. l_{p} measures the distance over which the orientation of the bonds is correlated, and can be estimated by averaging over all bonds:[34]

$$l_{\mathrm{p}} = -a/\ln\langle\cos(\theta)\rangle, \quad \text{(II.11)}$$

where a is the mean bond length ($a = 0.965\sigma$). To measure the persistence length of the chains for each k_{b}, separate simulations were performed in the absence of solvent and at low grafting density, to isolate the effect of the bending potential on the polymer rigidity. Then, the average of $\cos(\theta)$ over all bonds was taken, and eqn (II.11) was used to determine the value of l_{p}. As expected for $k_{\mathrm{b}} \gg k_{\mathrm{B}}T$, the relation $l_{\mathrm{p}} = k_{\mathrm{b}}\sigma/k_{\mathrm{B}}T$ can be used to estimate the persistence length.[35] In our case, the difference between the measured persistence length (eqn (II.11)) and the estimation yield values smaller than 4%.

Polymers were tethered by immobilizing a terminal bead on one of the walls of the slit like pore. A square lattice arrangement of the grafting sites was chosen over a random distribution, as used in other works.[14,25,36] This choice allows to avoid inhomogeneities that could cause spurious local effects on the system. The distance between nearest grafting sites (lattice constant, a_{l}) is related to the grafting density by $\rho_{\mathrm{g}} = 1/{a_{\mathrm{l}}}^2$. The particle–wall interactions were modeled by a purely repulsive smooth integrated Lennard-Jones potential:

$$U_{\mathrm{wall}}(z) = A_{\mathrm{wall}}\left[\left(\frac{\sigma}{z}\right)^9 + \left(\frac{\sigma}{z}\right)^3\right], \quad \text{(II.12)}$$

where $A_{\mathrm{wall}} = 3.2\varepsilon$.

The equations of motion were integrated using the velocity-Verlet algorithm with a time step $\mathrm{d}t = 2 \times 10^{-3}\tau$ for equilibrium simulations and $\mathrm{d}t = 2 \times 10^{-4}\tau$ for out-of-equilibrium simulations. 10^7 relaxation time steps were performed before measuring quantities, in order to achieve a stationary state in out-of-equilibrium simulations. In all cases, the instant mean kinetic energy in the directions perpendicular to the driving force was used to

monitor that the temperature was maintained to the desired value throughout the simulations.

$$\frac{1}{N_{\text{part}}}\sum_{N_{\text{part}}}\frac{1}{2}mv_y^2 = \frac{1}{N_{\text{part}}}\sum_{N_{\text{part}}}\frac{1}{2}mv_z^2 = \frac{1}{2}k_{\text{B}}T \qquad \text{(II.13)}$$

In order to speed up the simulation time, the cell linked-list algorithm was used to reduce considerably the number of pairs needed to evaluate the interactions. This cell linked-list algorithm showed a better speed-up over the widely used Verlet list algorithm to loop over particle pairs, when the program is run in parallel in nodes with more than 12 cores. The parallelization of the code was implemented only to the force double loop, with a shared memory scheme in OpenMP.

The size of the simulation box was set to $L_x = 49\sigma$, $L_y = 28\sigma$ and the inter-wall distance was fixed at $L_z = 18\sigma$. In the directions parallel to the wall ($\hat{x}$ and $\hat{y}$) periodic boundary conditions were imposed to simulate a slit-like channel. The lateral dimensions of the box L_x and L_y were slightly adjusted when the grafting density was modified, to form a perfect lattice of grafting sites at the walls. The number of monomers per polymer chain was set to $N_{\text{mon}} = 16$, which gives a contour length of $l_c \simeq 15\sigma$ for the chains. With this choice of parameters, the condition $L_z < 2l_c$ is fulfilled, and the polymers tethered to opposing walls can get in contact, forming bundle structures across the channel. The number of solvent particles was set up to fill the channel at the thermodynamic equilibrium density for the liquid at the fixed temperature $\rho_s = 0.695\sigma^{-3}$.[31]

To drive the system out-of-equilibrium, an external constant force F_{ext} was applied on all particles of the system in a direction parallel to the walls ($\hat{x}$) of the nano-channel. The force induces a Poiseuille like flow of the free liquid solvent particles through the pore in a stationary regime. This corresponds to a pressure drop ΔP along the slit length L_x such that $F_{\text{ext}}\rho_s = \Delta P/L_x$. The range of forces used was $0 \leq F_{\text{ext}} \leq 0.02\varepsilon/\sigma$.

To analyze the structure of the polymeric bundles, the bidimensional radial distribution function $g(r)$ was calculated at $z = L_z/2$. This function is calculated by counting the mean number of neighboring monomers at a distance r, $r + \mathrm{d}r$, and height $L_z/2 - 0.25\sigma < z < L_z/2 + 0.25\sigma$, and dividing by the area of the annulus. To count the pair of particles only once, the radial distribution function is calculated for $r \leq 1/2\min(L_x, L_y)$.

III. Results

In Fig. 2 we show a typical density profile of the monomers and the liquid solvent in equilibrium and under solvent flow. The depicted system corresponds to a grafting density $\rho_g = 0.03\sigma^{-2}$, a solvent-monomer affinity $\varepsilon_{\text{ms}} = 1/3\varepsilon$, and a bending rigidity $l_p/l_c = 1$. The liquid occupies the center of the channel, away from the channel walls. The presence of polymers is higher near the walls due to the constrain of the tethered monomer albeit in equilibrium, some chains reach the center of the channel (upper panel in Fig. 2). Upon applying an external force, the monomer density profile is significantly modified (lower panel in Fig. 2). The presence of monomers in the middle of the channel disappears, and the polymers accumulate near the walls.

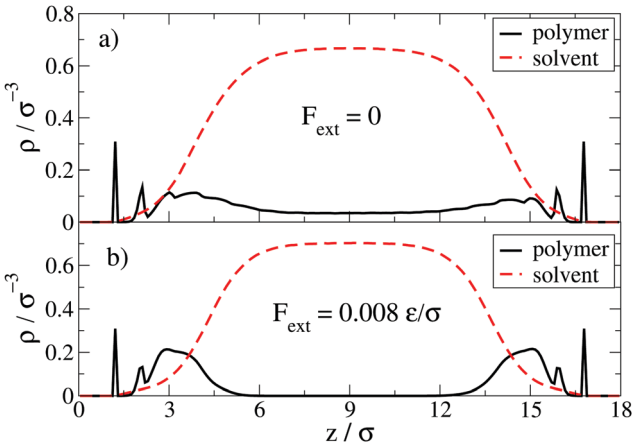

Fig. 2 Density profiles of the solvent (dashed line) and monomers of the brush (solid line). The profiles correspond to the same system (a) in equilibrium and (b) under an external driving force which produces solvent flow.

To elucidate the influence of these morphological changes in the flow, in Fig. 3 the flow rate is plotted against the external force. Error bars are omitted where data symbols are bigger than the statistical uncertainty throughout this work. Two distinct regimes are observed: one linear response for $F_{\text{ext}} < 0.004\varepsilon/\sigma$ and another regime in which the flow increases more rapidly with the external force for $F_{\text{ext}} > 0.004/\sigma$. These different responses of the system to the driving force correspond to two qualitatively different states of the nano-channel. For weak forces the top-grafted and bottom-grafted chains interact with each other, forming bundles of polymers which obstruct the flow, as shown in the left inset of Fig. 3. If the external force per particle is greater than a threshold ($F > F^* \equiv 0.004\varepsilon/\sigma$ in this case), the bundles break, and the channel opens, thus facilitating the flow of liquid, as depicted in the right inset of Fig. 3.

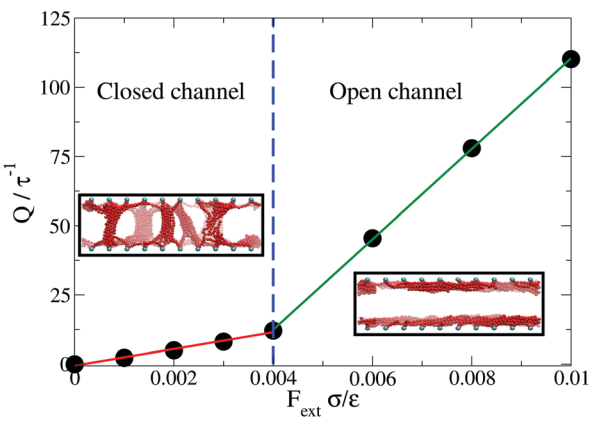

Fig. 3 Flow rate as a function of the external force applied on the system. A non-linear response of the system can be observed, due to the breaking of the bonds between top and bottom grafted polymers. The insets show a snapshot of the closed (left) and open (right) gate.

It is important to note that as usual brush methods of synthesis provide randomly grafted polymer layers, we also simulated this case, obtaining qualitatively similar results.

To quantify the effect of the switching state of the gate (open or closed), we introduce the dimensionless variable $\kappa = Q/Q_0$, known as permeability, where Q represents the mass flow rate through the channel and Q_0 is the mass flow rate with the closed channel. Q_0 is proportional to the applied external force, and the proportionality constant can be obtained by performing a linear regression of the mass flow rate as a function of F_{ext} for the closed gate regime, as shown in the red line in Fig. 3. Therefore, κ measures the change in the flow rate beyond the linear dependence on the driving force. A constant value of the permeability implies that there is no state change, while a sudden increase in κ shows a non-linear increase in the flow rate, suggesting an open gate state. It is worth mentioning that for every studied system, the flow rate increases linearly with the external force below the force threshold $F < F^*$.

A. Influence of chains stiffness

One of the distinctive elements of this work is the study of the response of a brush-coated nano-channel to liquid flow, as a function of the bending rigidity of the polymer chains. In Fig. 4, the flow rate (Q) is plotted as a function of the driving force (F_{ext}), for polymer brushes with different chain rigidities. The chain stiffness is characterized by the dimensionless quotient between its persistence length (l_p), and its contour length (l_c), as mentioned in Section II. The grafting density in this subsection is fixed at $\rho_g = 0.02\sigma^{-2}$, and solvent–monomer interaction parameter was set to $\varepsilon_{ms}/\varepsilon = 1/3$, which is a well studied set of parameters.[24,25] Firstly, we note that for fully flexible polymer brushes ($l_p/l_c = 0.1$) the flow rate increases linearly with the driving force, as expected in a Poiseuille flow (black curve in Fig. 4). Upon increasing the stiffness of the polymer chains, a non-linear response arises, as observed in the inset of Fig. 4. It is possible to discern the qualitatively different responses of the semi-flexible (blue) and the fully flexible (black) polymer brushes. For very stiff polymers ($l_p/l_c \geq 3$), the bundle structures are more robust, and do not break in the range of driving forces explored in this work (brown and turquoise curves).

Given the fact that the persistence length of the polymers plays an important role in the mechanical gating of the nano-channel, it is of interest to find the stiffness that maximizes the non-linear response. In Fig. 5 the normalized flow rate is plotted as a function of the persistence length of the chains, for two values of external force. To normalize each curve, the values are divided in each case by the flow rate of the system with the fully flexible polymer chains ($l_p/l_c = 0.1$). This normalization facilitates the visualization of the effect of the bending rigidity on the liquid velocity for the open and closed channel simultaneously. For small forces ($F < F^*$, red squares), the gate is closed, and the flow rate decreases with increasing bending rigidity. As the rigidity of the polymers grows, more chains reach the center of the channel, increasing the number of bundle structures, and thus reducing the flow rate. The behavior of the system is more complex when the forces are above the threshold, and the gate is open. In this case the mean velocity of the liquid has a non-monotonic dependence on the bending stiffness, achieving a maximum for polymers whose persistence lengths are equal to their contour length $l_p/l_c = 1$. A very interesting result from this graph is that when the channel is open, increasing the bending rigidity of the polymers enhances the flow of liquid across the channel, as long as $l_p/l_c \leq 1$. Increasing the bending rigidity over $l_p/l_c > 1$ hinders the solvent velocity, as already observed by Deng *et al. via* DPD simulations.[11]

To observe this effect experimentally it is necessary to use rather stiff polymers, given that typical persistence lengths of polymers are of the order of ~1 nm. One possible system could be assembled using short DNA chains ($l_c \sim 80$ nm and $l_p \sim 40$ nm)[37] in a narrow channel ($L_z \sim 100$ nm), with low grafting densities ($\rho_g \sim 0.003$ nm^{-2}). For electrokinetic flows, it is possible to narrow down the channel width to $L_z \sim 50$ nm,[38] where the effect is maximized with $l_p \sim l_c \sim 40$ nm. Other possible polymer is single-stranded DNA polyelectrolytes, whose effective

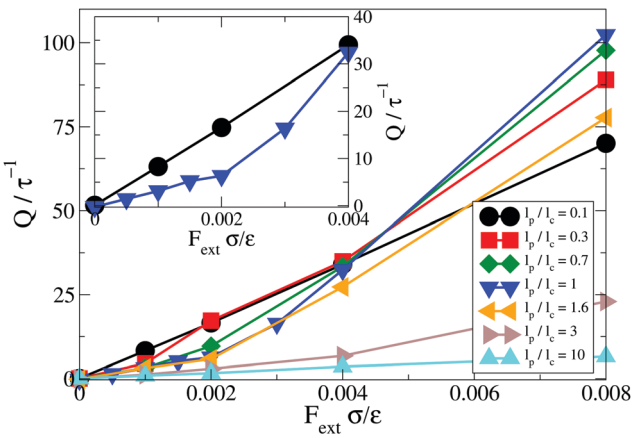

Fig. 4 Flow rate as a function of the external force, for various values of polymer bending rigidity. Inset: Close-up for the fully flexible (black dots) and semi-flexible (blue triangles) cases for better visibility. Lines are guides to the eye.

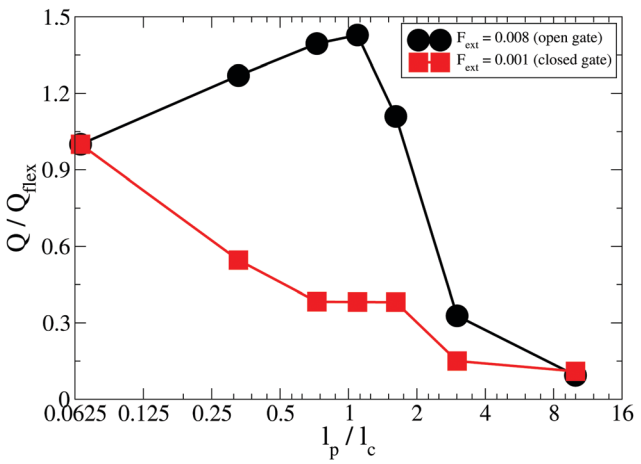

Fig. 5 Normalized flow rate as a function of persistence length l_p over contour length l_c of the polymers for the closed (red squares) and open (black circles) gate cases.

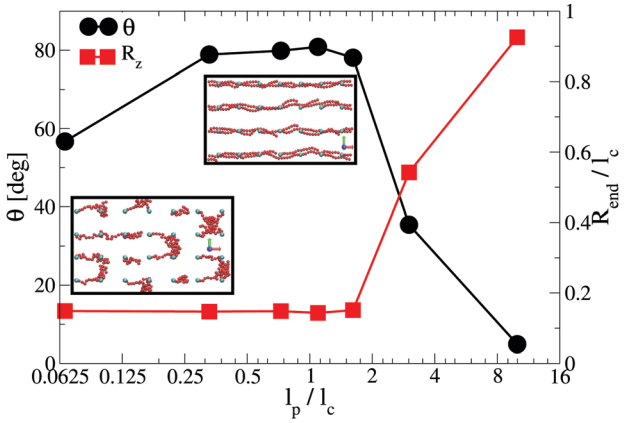

Fig. 6 Angle of inclination of the chains in the flow direction (black dots) and polymer extension perpendicular to the wall (red squares) as a function of bending rigidity, for the open gate ($F_{ext} = 0.008\varepsilon/\sigma$). Insets are top-view snapshots of the polymer brush. The lower left snapshot corresponds to $l_p/l_c = 0.1$ and the upper snapshot corresponds to $l_p/l_c = 1$.

thickness/stiffness could be varied with ionic strength.[39] They could also be selectively hybridized with complementary strands, leading to a large variation in persistence lengths.[40,41]

To comprehend this behavior it is necessary to look into the arrangement of the polymers, and how it affects the interaction with the fluid. The polymers' inclination angle in the flow direction and the chains' vertical component of the end-to-end vector are plotted as a function of the persistence length for an external force $F_{ext} = 0.008\varepsilon/\sigma$, in Fig. 6. We can observe that for $l_p/l_c \leq 1$, the brush height remains constant, while the inclination in the direction of the flow increases. This suggests that the increase in the flow rate in this range of rigidities ($l_p/l_c \leq 1$) is not due to a change in the brush height, but it is related to the alignment of the chains in the flow direction. The inclination of the chains in the flow direction presents a similar dependence to that of the flow rate for the whole range of bending rigidities explored. The correlation between chain inclination and flow was firstly observed by Qiao and He[27] in the context of electroosmotic flow in fully flexible neutral polymer brushes. The bending rigidity has an important role in the polymers alignment, because it favors the coherent orientation of consecutive bonds,[24] maximizing the chain elongation in the direction of the flow. If the distance between grafting points is smaller than the contour length of the semiflexible polymers, they will get in contact with the neighboring chains, forming stable arrays in the direction of the flow, as shown in the upper inset of Fig. 6. This particular morphology of the semiflexible polymers minimizes the liquid-brush interactions, thus decreasing the friction. On the other hand, fully flexible chains remain in the so called "mushroom regime" (see left inset of Fig. 6), which is more efficient in rendering drag to the liquid, reducing its velocity. Increasing the stiffness of the polymers beyond $l_p/l_c > 1$ hinders the inclination of the chains in the direction of the flow, and it enhances the elongation in the direction perpendicular to the walls, consequently slowing down the solvent velocity.

The bending rigidity of the polymer chains has a great influence on the arrangement of the bundles inside the nanochannel in equilibrium. For instance, fully flexible polymer brushes do not form bundle structures across the channel, while rigid polymer brushes form robust bundle structures that obstruct the solvent flow inside the channel. To gain insight into the structure of the polymeric bundles in the channel, the bidimensional radial distribution function $g(r)$ of the monomers at $z = L_z/2$ is plotted for various values of bending stiffness in Fig. 7. For fully flexible chains, there is no presence of monomers at half width of the channel, and of course there is no formation of bundle structures. As the bending rigidity increases, the number of bundle structures grows (see inset of Fig. 7), but the width of these structures does not change significantly (see red, green, blue and orange curves). For $l_p/l_c = 3$, the radial distribution function has a high peak around $r = 2\sigma$, which corresponds to the presence of second neighbors in the bundles. These wider structures are more stable, and are not broken as easily as the bundles formed by semiflexible polymers with $l_p/l_c < 3$. This can be observed in Fig. 5, where the flow rate decreases rapidly for $l_p/l_c = 3$, because the driving force is not enough to open the gate.

Another interesting element to observe in Fig. 7, is that for very rigid rods ($l_p/l_c = 10$) the bundles lack of a defined structure. This curve has a peak in the first neighbor, and then decreases without marked peaks. We think that the very rigid nature of these polymers inhibits the formation of stable wide bundle structures, as the chains are forced, due to the hard bending potential, to be oriented perpendicular to the wall. From the visual inspections of the simulations, we observe that these rigid polymers tend to form structures composed mainly of one top-grafted and one bottom-grafted polymer.

In the inset of Fig. 7 it is shown that the number of monomers in the center of the channel increases with the bending rigidity in a non-trivial way. For $l_p/l_c = 3$ the orientational correlation length of the bonds exceeds by far the contour

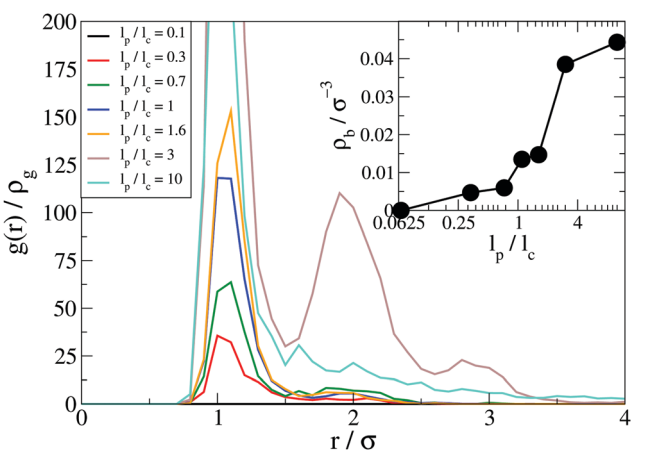

Fig. 7 Bidimensional radial distribution function of the monomers in the center of the nanochannel in equilibrium, for various bending rigidities. Inset: Monomer density in the center of the channel as a function of polymer stiffness, in equilibrium.

length of the chains, and there is a sudden increase in the presence of monomers in the middle of the channel.

B. Effect of grafting density

One experimentally accessible parameter of great interest is the number of tethered polymers per unit area (ρ_g). In Fig. 8(a) we show the permeability (κ) inside the channel as a function of the driving force, for various grafting densities. For these simulations, the bending constant used was the same for all grafting densities, and was set to fulfill the relation $l_p/l_c = 1$, which maximizes the gating response, as mentioned previously (see in Fig. 5). The solvent–monomer interaction parameter was fixed at $\varepsilon_{ms}/\varepsilon = 1/3$, as in the previous section. For $\rho_g < 0.11\sigma^{-2}$, the system behaves qualitatively in the same way: for small forces the flow rate increases slowly with the driving force, and after a certain threshold $F^*(\rho_g)$, which is different for each grafting density, the liquid velocity grows rapidly as the external force increases. For $\rho_g \geq 0.11\sigma^{-2}$, the bundle structures do not break in the range of forces explored in this work, thus there is no change in the behavior of the system. As observed by Huang *et al.*,[19] by Li *et al.*[22] and Zuo *et al.*[4] for fully flexible polymers, the channel permeability is reduced as the grafting density is increased.

It is interesting to see how these changes of behavior of the flow correlate with a sudden decrease in the polymer brush height, as seen in the right panel of Fig. 8. Firstly, we can observe from this plot, that the brush height increases with grafting density, and decreases with the pressure gradient, as observed experimentally by Castro *et al.*[28] Secondly, each grafting density has a force intensity threshold F^*, at which the top–bottom polymer grafted interactions break, leaving a portion of the channel unobstructed and favoring the flow of liquid. As the polymeric structures break, the chains lean in the direction of the flow, and abruptly contract to the grafted walls. We observe clearly that upon increasing the grafting density (ρ_g), the necessary force to break the top–bottom bonds (F^*) also increases.

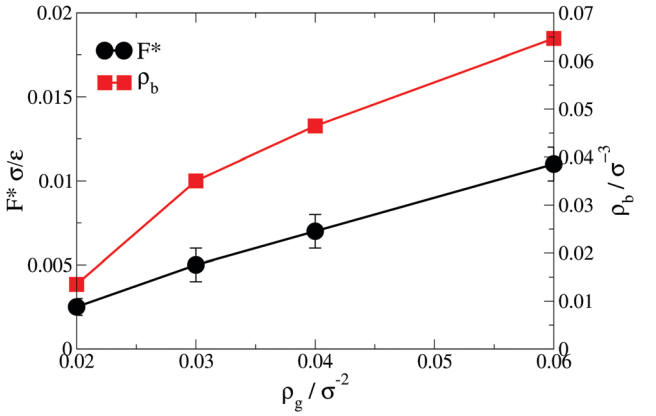

Fig. 9 Critical force (black dots) and bundle density in the middle of the channel (red squares) as a function of grafting density.

To quantify the influence of the grafting density on the force threshold (F^*), in Fig. 9 we plotted F^* against ρ_g (black dots). To estimate the value of F^* for each grafting density, we have taken the value at which the curve R_z in Fig. 8(b) crosses the average of R_z with the gate open and R_z with the gate closed. The threshold force increases with the number of grafted chains, as expected. As we add polymers to the system, the top and bottom grafted chain interactions increase, thus incrementing the necessary force to break the bundle structures formed in equilibrium. F^* and ρ_g present a rather linear behavior. We can think on F^* as the force needed to break the pairs of "bonded" monomers. These can be defined as a pair of monomers belonging one to a chain of the upper wall, and the other to a chain of the lower wall, which from a bundle (see Fig. 1, upper panel). For constant stiffness, the linear behavior would indicate that the number of pairs of bonded monomers N_{bonded} increases linearly with the grafting density: $N_{bonded} \sim N_g \sim \rho_g$, where N_g is the number of grafted chains in each wall. This seems reasonable for relatively stiff chains and it is further supported by observing how the monomer density in the middle of the

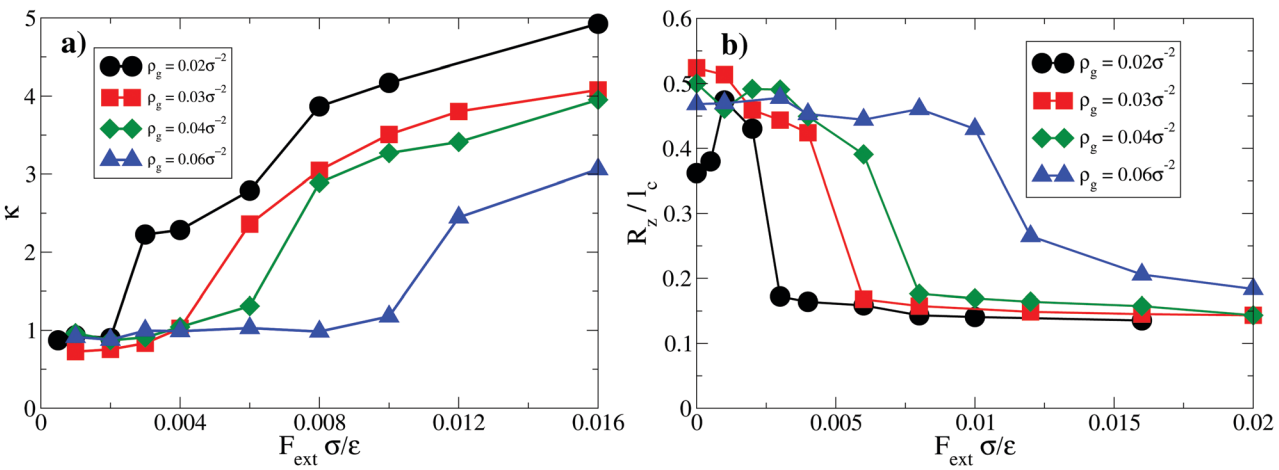

Fig. 8 (a) Permeability (κ) as a function of the external force F_{ext}, for various grafting densities. (b) Mean polymer extension in the direction perpendicular to the walls as a function of the external driving force, for various grafting densities.

channel grows with the grafting density (red squares in Fig. 9). For $\rho_g \geq 0.03\sigma^{-2}$ the number of monomers in the middle of the channel increases linearly with ρ_g.

C. Dependence on solvent quality

Lastly, we investigate the behavior of the system for different solvent–polymer affinities, ranging from good to poor solvent conditions. Changing the solvent quality at constant pressure difference is a well-known method to switch the gating state in nano-channels.[18–21,42,43] In this sub-section we study flow rate response by varying the driving force, for different solvent qualities. The monomer-liquid interaction was modified by changing the value of ε_{ms} in eqn (II.7). The values used for this parameter were $\varepsilon_{ms} = 1\varepsilon$, which corresponds to good solvent conditions, $\varepsilon_{ms} = 0.66\varepsilon$, and $\varepsilon_{ms} = 0.33\varepsilon$, which implies a high incompatibility between polymers and liquid. To complete the study as a function of solvent quality, a purely repulsive interaction between monomers and liquid was implemented to include the limiting case of ideal poor solvent. We set the cut-off radius of the monomer–solvent interaction to $r_C = \sqrt[6]{2}\sigma$, while the cut-off was kept at $r_C = 2\sqrt[6]{2}\sigma$ for monomer–monomer and solvent–solvent interactions. The bending constant was set, as in the previous sub-section, so that the persistence length of the polymer is equal to its contour length $l_p/l_c = 1$, which maximizes the gating response of the system, while the grafting density was fixed at $\rho_g = 0.02\sigma^{-2}$.

In Fig. 10 the permeability $\kappa = Q/Q_0$ is plotted as a function of the external driving force F_{ext} for various solvent conditions. For good solvent conditions, the interactions between monomers of different polymers is equal to the interaction between solvent particles and monomers, which inhibits the formations of bundles. The absence of this structures in the channel for the good solvent case (blue symbols in Fig. 10), is reflected by the flat response of the permeability to the driving force. On the other side, the ideal poor solvent case (black circles) exhibits a huge boost in the permeability (κ) as F_{ext} increases and the polymeric bundle structures that obstruct the channel break. As the incompatibility between solvent and brush increases, the non-linear response of the flow is more appreciable, in agreement with the independent simulation studies performed by Adiga and Brenner[18] and Huang *et al.*[19] This behavior disagrees with the self-consistent study made by Suo *et al.*,[21] where they observe a decrease in permeability due to an increase in the brush height as the pressure drop increases.

To gain insight into the behavior of the system, it is convenient to analyze the morphological changes of the polymer brush. In Fig. 11, the average height of the brush is plotted against the driving force for all the explored solvent qualities. As also observed by Posel *et al.*,[20] a high negative correlation between the brush height and the channel permeability shows up when varying the solvent quality. For high brush–solvent affinities (good solvent), the brush height varies smoothly with the external force. Similar results were observed by Adiga and Brenner, when computing the brush height as a function of shear rate in good solvent conditions (see Fig. 5 of ref. 18). For low affinities (poor solvent), there is a sudden decrease of the mean polymer extension upon increasing the shear rate. This result contrasts with the observations from Huang *et al.*,[19] that in poor solvent regime, the brush height is not significantly affected by the driving force of the flow. However, it is worth mentioning that the grafting densities used in their work are considerably higher than those explored in this work, and they use fully flexible polymers, while in this work we use semi-flexible chains.

From the plot in Fig. 11, we can observe that the chemical incompatibility between solvent and brush is a key element for the gating phenomena to take place. The brush height decreases as the solvent quality gets poorer, due to the contraction of the chains, as observed experimentally.[44] It is also interesting to note that the value of the critical force F^* at which the bundles break, does not depend significantly on the solvent quality.

To study the structure of the polymeric bundle formations in equilibrium, in Fig. 12 we present the bidimensional radial distribution function ($g(r)$) of monomers in the center of the channel ($z = L/2$), for different solvent qualities (see last paragraph

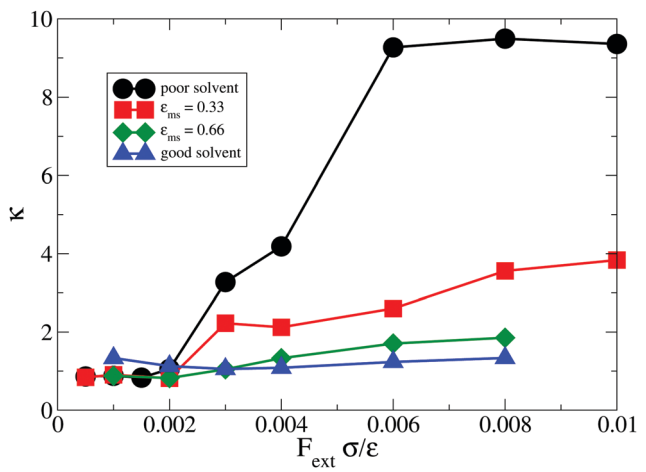

Fig. 10 Permeability of the systems for various values of solvent quality, as a function of the external force.

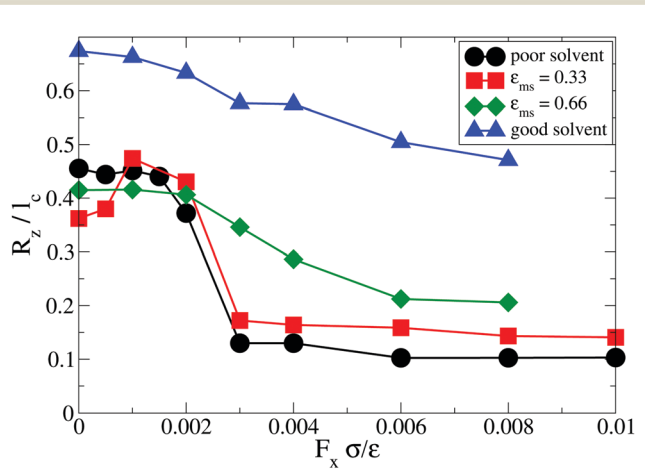

Fig. 11 Average extension of the polymers in the direction perpendicular to the walls as a function of the driving force, for various solvent qualities.

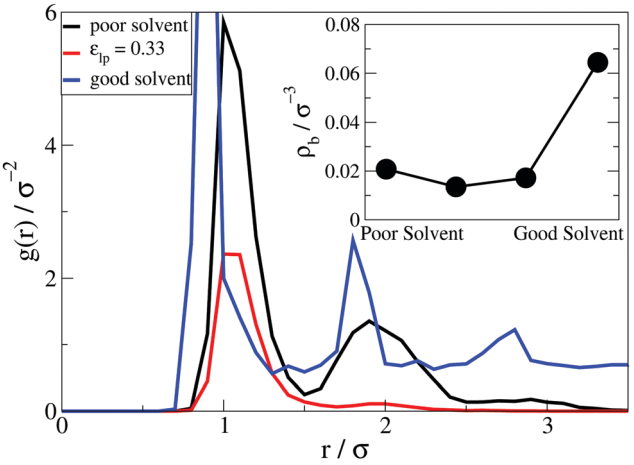

Fig. 12 Bidimensional radial distribution function for the monomers at $z = L/2$ (center of the channel), for various solvent qualities. Inset: Monomer number density in the center of the channel ($L_z/2 - 2\sigma < z < L_z/2 + 2\sigma$) as a function of solvent quality.

of Section II for details of the calculation). A high presence of monomers in the center of the channel is observed for good solvent (see inset of Fig. 12), but there is a difference in structure. In this case, there is no formation of static structures, and the polymers are dynamically rearranging themselves over time. As the solvent quality gets poorer (red line in Fig. 12), the polymers form bundles, and there is little rearranging of this structures in time. For the poorest solvent quality (black line in Fig. 12), we can observe that the second peak is higher than the intermediate case (red line), which shows that the bundles get wider upon lowering the solvent–polymer affinity from $\varepsilon_{ms} = 0.33\varepsilon$ to the ideal poor solvent case. The increase in the monomer density in the middle of the channel can be also observed in the inset of Fig. 12.

IV. Concluding remarks

We performed coarse grained molecular-dynamics simulations of solvent flowing through a slit like-channel grafted with semiflexible polymer brushes. The walls of the nano-channel were located close enough to each other, allowing for a direct interaction among polymers tethered to opposing walls. For low solvent–polymer affinity, the formation of stable bundle-like structures in equilibrium across the channel was observed. After studying the system in equilibrium, a Poiseuille flow was induced by applying a constant force on all particles. For a limiting threshold force F^* the bundle structures break, leaving the middle of the channel free of obstructions, which abruptly enhances the flow rate. The system switches from a low flow rate to a high flow rate after imposing a sufficiently large pressure gradient. We examined the gating process by varying different physical properties of the system and found values that maximize the sensitivity of the system.

We explored the effects of the bending rigidity of the polymers. The influence of the stiffness on the flow was characterized for a wide range of persistence lengths ($0 < l_p/l_c \leq 10$), from fully flexible chains to rigid rods. The configurational entropy makes the fully flexible chains to contract near the grafted walls, and they do not reach the chains from opposing walls, which leads to the inhibition of the gating process. On the opposite limit, rigid rods form very stable bundle structures across the channel, which did not break in the force range explored in this work. This also leads to a linear response of the flow as a function of the pressure gradient. The optimum gating response of the system was observed for semiflexible polymers with $l_p/l_c \simeq 1$. This is due to the ability of these chains to bend coherently, opening the channel for unobstructed flow of solvent. When the channel is open, we observe a high correlation between the angle of inclination of the chains in the direction of the external force and the flow rate.

We also varied the grafting density (ρ_g), leaving $l_p/l_c = 1$ and the solvent quality ($\varepsilon_{ms}/\varepsilon = 1/3$) constants. Upon increasing ρ_g, the force threshold (F^*) at which the gate opens becomes greater. Furthermore, the relation between F^* and ρ_g appears to be linear in the explored range. This suggests a convenient way to design a pressure sensor that abruptly enhances the flow at a precise pressure drop, which can be tuned with the grafting density. The qualitative response of the flow as a function of the driving force does not change significantly with the grafting density. We find the height of the brush to be a good indicator of the open/closed state of the channel.

Lastly, the effect of the solvent quality was examined. The chemical incompatibility between solvent and brush was found to be a key element for the gating phenomena to take place. In poor solvent conditions, the top and bottom grafted polymers bond with each other, forming bundles in the center of the channel, consequently hindering the flow of the solvent in the presence of a driving force. Upon increasing the external force, the bundle structures break, and the polymers lean in the direction of the flow, leaving the center of the channel free, which abruptly enhances the permeability of the channel. Upon improving the solvent quality, the bundle structures become narrower and relation between high and low flow rate states becomes flatter. We expect that these results will motivate further experimental work to explore the possibilities of these phenomena in microfluidic developments.

Conflicts of interest

There are no conflicts to declare.

Acknowledgements

Financial support through grants PIP 11220150100417 (CONICET), BAPIN 2014, BAPIN 2017 (CNEA), PME 0129-2015, PICT-E 134-2014 (MINCYT) is gratefully acknowledged.

References

1 O. Azzaroni, *J. Polym. Sci., Part A: Polym. Chem.*, 2012, **50**, 3225.
2 N. Fortin and H.-A. Klok, *ACS Appl. Mater. Interfaces*, 2015, **7**, 4631.

3 B. Yameen, M. Ali, R. Neumann, W. Ensinger, W. Knoll and O. Azzaroni, *J. Am. Chem. Soc.*, 2009, **131**, 2070.
4 Y. Zuo, G. Wang, Y. Yu, C. Zuo, L. Shi, F. Shi and J. Wei, *J. Macromol. Sci., Part B: Phys.*, 2017, **56**, 26.
5 B. Yameen, M. Ali, R. Neumann, W. Ensinger, W. Knoll and O. Azzaroni, *Small*, 2009, **5**, 1287.
6 S. P. Adiga and D. W. Brenner, *J. Funct. Biomater.*, 2012, **3**, 239.
7 R. Duan, F. Xia and L. Jiang, *ACS Nano*, 2013, **7**, 8344.
8 H. Liu, Y. Li, K. Sun, J. Fan, P. Zhang, J. Meng, S. Wang and L. Jiang, *J. Am. Chem. Soc.*, 2013, **135**, 7603.
9 G. Jeon, S. Y. Yang and J. K. Kim, *J. Mater. Chem.*, 2012, **22**, 14814.
10 E. R. Cruz-Chu, A. Malafeev, T. Pajarskas, I. V. Pivkin and P. Koumoutsakos, *Biophys. J.*, 2014, **106**, 232.
11 M. Deng, X. Li, H. Liang, B. Caswell and G. E. Karniadakis, *J. Fluid Mech.*, 2012, **711**, 192.
12 S. Weinbaum, J. M. Tarbell and E. R. Damiano, *Annu. Rev. Biomed. Eng.*, 2007, **9**, 121.
13 X. Z. Jiang, H. Gong, K. H. Luo and Y. Ventikos, *J. R. Soc., Interface*, 2017, **14**, 20170780.
14 F. Römer and D. A. Fedosov, *EPL*, 2015, **109**, 68001.
15 L. Lanotte, G. Tomaiuolo, C. Misbah, L. Bureau and S. Guido, *Biomicrofluidics*, 2014, **8**, 014104.
16 S. P. Adiga and D. W. Brenner, *Macromolecules*, 2007, **40**, 1342.
17 S. P. Adiga and D. W. Brenner, *Nano Lett.*, 2002, **2**, 567.
18 S. P. Adiga and D. W. Brenner, *Nano Lett.*, 2005, **5**, 2509.
19 J. Huang, Y. Wang and M. Laradji, *Macromolecules*, 2006, **39**, 5546.
20 Z. Posel, M. Svoboda, C. M. Colina and M. Lisal, *Soft Matter*, 2017, **13**, 1634.
21 T. Suo and M. D. Whitmore, *J. Chem. Phys.*, 2014, **140**, 114902.
22 N. Li, C. Zuo and Q. Cao, *J. Macromol. Sci., Part B: Phys.*, 2012, **51**, 275.
23 T. Lee, S. C. Hendy and C. Neto, *Macromolecules*, 2012, **45**, 6241.
24 K. Speyer and C. Pastorino, *Soft Matter*, 2015, **11**, 5473.
25 K. Speyer and C. Pastorino, *Langmuir*, 2017, **33**, 10753.
26 A. Milchev and K. Binder, *EPL*, 2013, **102**, 58003.
27 R. Qiao and P. He, *Langmuir*, 2007, **23**, 5810.
28 R. P. Castro, H. G. Monbouquette and Y. Cohen, *J. Membr. Sci.*, 2000, **179**, 207.
29 C. Pastorino, Y. Kim, S. Minko and M. Müller, *Macromolecules*, 2018, **51**, 6387.
30 P. E. Nol and P. Warren, *Europhys. Lett.*, 1995, **30**, 191.
31 M. Müller and L. G. MacDowell, *Macromolecules*, 2000, **33**, 3902.
32 G. S. Grest and K. Kremer, *Phys. Rev. A: At., Mol., Opt. Phys.*, 1986, **33**, 3628.
33 K. Kremer and G. S. Grest, *J. Chem. Phys.*, 1990, **92**, 5057.
34 A. Nikoubashman, A. Milchev and K. Binder, *J. Chem. Phys.*, 2016, **145**, 234903.
35 H.-P. Hsu, W. Paul and K. Binder, *Macromolecules*, 2010, **43**, 3094.
36 P. R. Desai, S. Sinha and S. Das, *Soft Matter*, 2017, **13**, 4159.
37 P. Gross, N. Laurens, L. B. Oddershede, U. Bockelmann, E. J. G. Peterman and G. J. L. Wuite, *Nat. Phys.*, 2011, **7**, 731.
38 K. P. Lee, H. Leese and D. Mattia, *Nanoscale*, 2012, **4**, 2621.
39 N. M. Toan and C. Micheletti, *J. Phys.: Condens. Matter*, 2006, **18**, S269.
40 A. Bosco, F. Bano, P. Parisse, L. Casalis, A. DeSimone and C. Micheletti, *Nanoscale*, 2012, **4**, 1734.
41 G. Doni, M. D. Nkoua Ngavouka, A. Barducci, P. Parisse, A. De Vita, G. Scoles, L. Casalis and G. M. Pavan, *Nanoscale*, 2013, **5**, 9988.
42 Y. Ito, Y. S. Park and Y. Imanishi, *Langmuir*, 2000, **16**, 5376.
43 O. Peleg, M. Tagliazucchi, M. Kröger, Y. Rabin and I. Szleifer, *ACS Nano*, 2011, **5**, 4737.
44 A. N. Constable and W. J. Brittain, *Colloids Surf., A*, 2011, **380**, 128.